Title

Base-level lowering rates control a landslide process transition in California's Franciscan mélange

ISBN
9798190917604

Author
Fakrai, Nessa

Publication Date
2026-08-26

UNIVERSITY OF CALIFORNIA

SANTA CRUZ

BASE-LEVEL LOWERING RATES CONTROL A LANDSLIDE PROCESS TRANSITION IN CALIFORNIA'S FRANCISCAN MÉLANGE

A thesis submitted in partial satisfaction
of the requirements for the degree of

MASTER OF SCIENCE

in

EARTH SCIENCES

by

Nessa Salma Fakrai

September 2026

The Thesis of Nessa Salma Fakrai is approved:

____
Professor Noah J. Finnegan, Chair

____
Dr. Jonathan P. Perkins

____
Professor Jeremy K. Hourigan

____
Peter Biehl
Vice Provost and Dean of Graduate Students

TABLE OF CONTENTS

LIST OF FIGURES

LIST OF TABLES

ABSTRACT

BASE-LEVEL LOWERING RATES CONTROL A LANDSLIDE PROCESS TRANSITION IN CALIFORNIA'S FRANCISCAN MÉLANGE

Nessa Salma Fakrai

California's Franciscan mélange is well-known for hosting persistent, slow-moving earthflows, a landslide style favored by the unit's significant local variability in shear strength (e.g. Medley, 2001; Kim et al., 2004; Roering et al., 2015). Big Sur's mélange, however, is unusual: landslide mapping there reveals both recent (e.g. the 2017 Mud Creek landslide) and prehistoric rotational landslides on slopes that are unusually steep for this lithology. Because rotational landslides and earthflows pose markedly different hazards, understanding what drives the shift in failure style is critical for hazard assessment. Here we test the hypothesis that the rate of base-level lowering governs the transition between earthflow and rotational failure. We synthesize landslide mapping and analysis of high-resolution topography across two Franciscan mélange settings with contrasting rates of base-level lowering: the South Fork Eel River canyon, where river incision drives base-level lowering at ~1 mm/yr, and the southern Big Sur coast, where wave erosion drives local base-level lowering at ~2 cm/yr. We then use 2-D numerical modeling to test whether rapid coastal retreat alone can drive a transition from earthflow to rotational failure in a Franciscan mélange hillslope.

Landslide mapping shows that landslide activity in Big Sur, as defined by InSAR-derived deformation rates, is concentrated along the actively eroding coastline, and that the two regions differ systematically in failure style according to overall hillslope angle. Big Sur's steeper slopes are dominated by rotational landslides, while the Eel River region's shallower slopes are dominated by earthflows. Numerical modeling shows that progressive lateral erosion can produce rotational failure on hillslopes that were previously deforming as earthflows, provided there is some degree of vertical heterogeneity in the weathering profile. Taken together, these results indicate that changes in the rate of base-level lowering can drive wholesale shifts in landslide failure style and hazard, likely mediated by long-term coupling between base level and hillslope weathering.

INTRODUCTION

Background and Motivation

Landslides, or the mass mobilization and downslope transport of rock, soil, and fluids, are natural hazards that can pose major threats to life, property, and infrastructure. With the progression of climate change, catastrophic landslide events are expected to increase in frequency and severity (e.g. Gariano and Guzzetti, 2016; Warrick et al., 2019; Dickson et al., 2007; Dawson et al., 2009) requiring affected communities to undertake prolonged and costly cleanup endeavors (Walkinshaw, 1992). In California, many of these landslides are focused within the mélanges of the Franciscan Complex, an assemblage of deformed and metamorphosed accretionary wedge rocks originating from the ancient subduction zone along California's continental margin (Berkland et al., 1972; Raymond, 2018; Handwerger et al., 2022; Xu et al., 2021). These Cretaceous-aged mélanges are heavily sheared and have a clay-rich matrix (Figure 1a-b) but have stabilizing blocks within, meaning the Franciscan mélange has extreme local variability in shear strength (Medley, 2001; Kim et al., 2004; Lindquist and Goodman, 1994). The weakness of the mélange matrix coupled with its persistently elevated pore fluid pressures (e.g., Hahm et al., 2019), makes it an ideal medium for landslide initiation, and indeed, actively moving landslides across California occur in regions of Franciscan mélange (Handwerger et al., 2022; Figure 1c-d).

Within the Franciscan mélange, the most common landslide failure style is that of an earthflow (Roering et al., 2015): a persistent, slow-moving (<4 m/yr) landslide which often activates on planar and generally shallow slopes (~15-20º), within fine-grained, weathered lithologies (e.g. Keefer and Johnson, 1983; Kelsey, 1978). Earthflows typically deform in a visco-plastic manner (e.g. Hungr et al., 2014; Mackey and Roering, 2011; Kelsey, 1978; Ohlmacher, 2007), a process that often speeds up in response to seasonal changes in pore-water pressure (e.g., Iverson and Major, 1986; Handwerger et al., 2013; Finnegan et al., 2021). In certain cases, Franciscan mélange can also host deeper slow-moving landslides that are morphologically distinct from earthflows in overall slope and aspect ratio, to name a few. Whereas earthflows are not typically seen as threats to human life, their persistent movement can impact property and infrastructure (e.g., Bertolini et al., 2005; Mansour et al., 2011). The 2019 Hooskanaden landslide in southern Oregon, for example, shut down a section of US Highway 101 for nearly 2 weeks (Alberti et al., 2020). Conversely, some deeper slow-moving landslides may experience a shift from steady seasonal deformation to rapid, catastrophic failure (e.g. Lacroix et al., 2020; Handwerger et al., 2016, 2019).

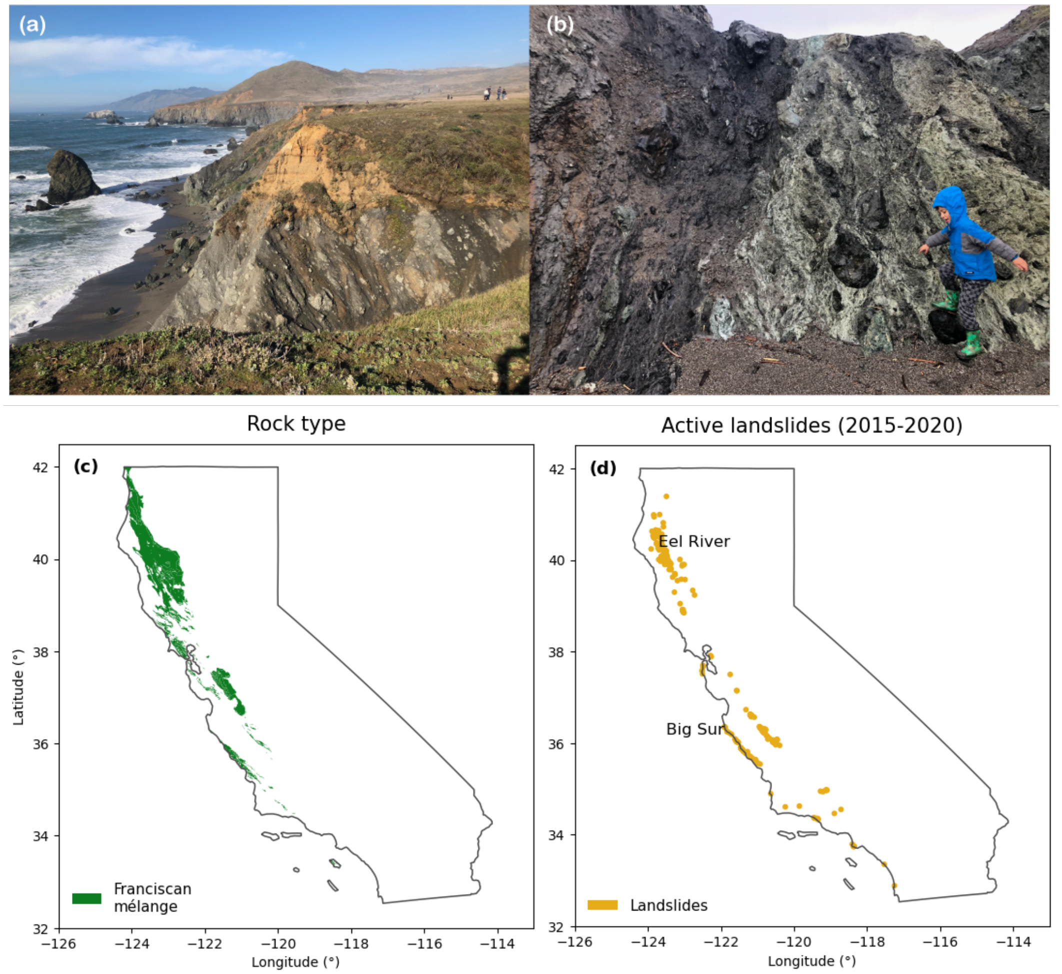

Figure 1. Cretaceous-aged Franciscan mélange rocks: **(a)** An outcrop showing "block-in-matrix" fabric of mélange, characterized by large, competent blocks in a pervasively sheared argillite matrix (photo by Noah Finnegan); **(b)** A zoomed-in view of the block-in-matrix fabric (photo by Noah Finnegan); **(c)** (adapted from Handwerger et al., 2022) Simplified geologic map showing the area extent of the Franciscan mélange rock unit; **(d)** (adapted from Handwerger et al., 2022) Locations of active landslides identified from interferometric synthetic aperture radar (InSAR) analyses.

Through the Big Sur region of California's central coast, Highway 1 (also known as the Pacific Coast Highway) traverses terrain largely underlain by Franciscan mélange (Figure 2a). This area has suffered repeated and prolonged landslide-related road closures that severely impact the local communities, whose economy relies heavily on tourism drawn by the scenic highway (Beacon Economics, 2025). Since its construction in the 1920s and 1930s, Highway 1 has been closed more than fifty times because of landslide damage (Handwerger et al., 2019; JPR Historical Consulting Services, 2001). While most of the landslide activity on the Big Sur coast is due to slow landslides (e.g., Desai et al., 2025), a notable exception is the 2017 Mud Creek landslide (Figure 2b), a rotational landslide that failed catastrophically after creeping for years. The Mud Creek failure displaced an estimated 4-6 million cubic meters of material and destroyed nearly half a kilometer of roadway, closing the Highway 1 corridor through Big Sur for over a year (California Department of Transportation, 2018). Preliminary head scarp fractures formed in early May of 2017, and the main failure event occurred a few weeks later. Importantly, Mud Creek did not suddenly activate in 2017; it had been deforming slowly for eight years prior to its catastrophic collapse (e.g. Handwerger et al., 2019; Warrick et al., 2019; Jacquemart and Tiampo, 2021). In other words, unlike in other areas of Franciscan mélange, Big Sur's mélange rocks are apparently capable of transitioning from a slow-moving creep regime to a rapid failure regime within remarkably short timescales. Landslide mapping in the region (Fakrai and Perkins, 2026) also provides topographic evidence for similar but prehistoric catastrophic landslides. This observation motivates the two central questions of this study: 1) What controls the transition from earthflow-dominant to rotational-landslide-dominant terrain within the Franciscan mélange and 2) how does this impact regional landslide hazard?

A more complete understanding of landslide hazards (and indeed frictional behavior more generally) within mélange rock requires quantifying the controls on landslide failure process transitions. Towards that end, a key difference between the Big Sur coast, where the catastrophic Mud Creek failure occurred, and the classic "melting ice cream" terrane along the Eel River where earthflows have been extensively studied (Kelsey, 1978; Mackey and Roering, 2011, Roering et al., 2015), is the erosional boundary condition acting on hillslopes. Landslide activity in mountainous regions can be tied to the rates of adjacent river incision which set the lower boundary condition for slope stability by increasing both hillslope relief and gradient (e.g. Burbank et al., 1996, Schmidt and Montgomery, 1995). In coastal terrains, fluvial incision rates may also increase as wave-driven lateral erosion locally steepens channel mouths (e.g. Limber et al., 2018). Moreover, along the Big Sur Coast, rates of coastal erosion averages ~2 cm/yr (Dow et al., 2026), corresponding to similar rates of base-level lowering along steep coastal bluffs. In contrast, the Eel River has rates of vertical incision of up to ~ 1 mm/yr (Bennett et al., 2016; Roering et al., 2015). How does this order of magnitude difference in base-level lowering rates influence landslide processes?

This study compares lidar-derived and airborne synthetic aperture radar-derived landslide inventories in the contrasting landscapes of southern Big Sur, California and the middle fork of the Eel River in Humboldt County, California. To identify landslide process transitions in our inventories, we use topographic metrics to define rotational landslides and earthflows via their morphometric parameters (downslope aspect ratio and average deposit slope). We then perform a 2-D slope stability analysis to evaluate how wave erosion and the pattern of hillslope strength influences whether a hillslope is more likely to generate an earthflow or a deep, rotational failure. Finally, from these results, we propose a hypothesis regarding rates of base-level lowering and coastal erosion as potential drivers for these processes.

Description of Study Sites

1. Big Sur

Big Sur is a stretch of California's central coast that spans from Carmel-by-the-sea to the north through San Simeon to the south (Figure 2). Our study area is located at the southern end of Big Sur, spanning about 25 kilometers of coastline on the border of Monterey and San Luis Obispo counties (Figure 2a). The study area comprises three main watersheds, Willow Creek, Villa Creek, and Alder Creek (listed from northernmost to southmost), and covers a total of about 80 square kilometers.

A contact between two main lithologies latitudinally bisects the study area, with Broken Formation (Kjfb) in the north and Franciscan mélange (Kfm) in the south. Franciscan mélange is defined as sheared black and gray argillite enclosing blocks of greywacke, conglomerate, greenstone, diabase, chert, serpentinite, and glaucophane schist ranging in size from pebble to hill sized (Johnston et al., 2019).

Broken Formation is said to resemble Franciscan mélange in most ways but is distinguished by the lack of exotic blocks and a paucity of chert and basalt (Graymer et al., 2014). This area is tectonically active, experiencing ongoing uplift driven by compression and oblique motion from the San Andreas fault and San Gregorio-Hosgri fault systems located just inland of the study area (Young and Hilley, 2018; Johnson et al., 2018), which, together with wave-driven coastal erosion (Dow et al., 2026), sets the region's high relief and steep hillslope gradients. ^{10}Be concentrations in sediments from coastal watersheds north of the study area suggest basin-averaged erosion rates of ~0.07-0.4 mm/yr (Young and Hilley, 2018). That said, measurements of coastal cliff retreat rates of ~2 cm per year (Dow et al., 2026) suggest that near the coast, erosion rates might be much higher than what is revealed by basin-averaged values. This is also hinted at in Apatite and Zircon (U-Th)/He cooling ages, which are very young along the Big Sur coast, suggesting locally higher exhumation rates compared to basin-averaged, cosmogenic isotope derived values (Ducea et al., 2003; Steely, 2016; Young and Hilley, 2018). The Santa Lucia Mountains, stretching along the majority of the central coast, is an assemblage of ridges generally trending northwest-southeast with impressively high relief; the main ridge of the Santa Lucia Mountains, the Coast Ridge, is never more than 11 km away from the coastline, forming the steepest coastal slope in the contiguous United States (Henson and Usner, 1993).

Big Sur's climate is Mediterranean, characterized by precipitation mainly in the winter months and mild temperatures year around. Because of the area's drastic topography, precipitation rates (up to 80 cm per year; Hapke and Green, 2005) can vary significantly between high and low elevations, with the highest elevations experiencing as much as 3-4 times more precipitation than lower elevations during the winter (Henson and Usner, 1993). Additionally, annual precipitation fluctuates because of El Niño-Southern Oscillation events (Hapke and Green, 2006). These variations greatly affect landslide risk: the 2017 Mud Creek landslide occurred after a transition from historic drought conditions in Water Year 2016 to one of the wettest winters on record in Water Year 2017 (Handwerger et al., 2019). Further, wave action on Big Sur's coast can precondition slopes for rainfall-induced landsliding (e.g. Dow et al., 2026). Big Sur's continental shelf is steep and narrow compared to the shelf along other areas of the central coast (California Coastal Commission, 1987) and as waves travel across the narrow continental shelf, deep-water wave energy may not dissipate as readily as in areas with wider and more shallowly sloping continental shelves (Komar, 1998). Indeed, the shoreline is then subject to high-energy wave impacts from winter storm surges, promoting coastal retreat and hillslope steepening (Hapke et al., 2004).

Slow moving landslides are the predominant mode of mass wasting in Big Sur, determined from analyses of surface displacement derived from interferometric synthetic aperture radar (InSAR) (Winter et al., 2024). Hapke, Green, and Dallas (2004) identified active landslide motion in Big Sur by finding "recent disturbance" (i.e. lack of vegetation and clear landslide scars) in digital orthophotoquadrangles from 1994 and georeferenced imagery of the Big Sur coast from 1942 and 1929 and found that much of the region was actively deforming during the construction of Highway 1 in 1929. The only catastrophic landslide events in Big Sur in the last decade have been the 2017 Mud Creek landslide, the 2021 Rat Creek landslide, and the 2023-2024 Regents slide, which all collapsed directly onto Highway 1 causing prolonged road closures. Studies have shown also that landslides preferentially form in the softer, highly sheared rocks of the Franciscan mélange rather than in the more competent sedimentary and granitic rocks (e.g. Hapke et al., 2004).

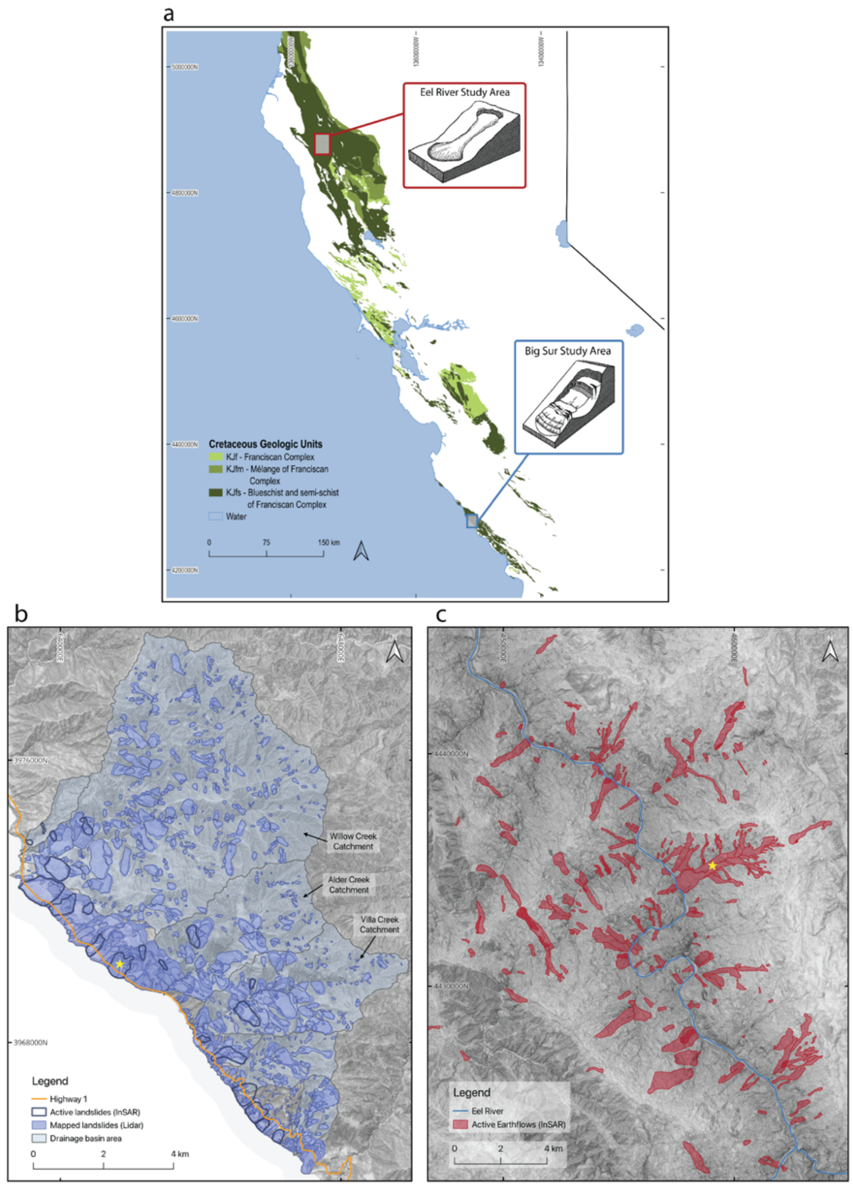

Figure 2: **(a)** Location of Big Sur (south) and Eel River (north) study areas shown with mélange unit extents as well as the more common local landslide failure mode; **(b)** Big Sur landslide inventory. Lidar- derived landslide polygons are shown in semi-transparent blue (Fakrai and Perkins, 2026) and InSAR-derived active landslide polygons (Winter et al., 2024) are shown in heavyweight dark blue outline; Highway 1 road line is shown in yellow-orange; drainage basin areas/study area boundaries are shown in semi-transparent light blue; 2017 Mud Creek landslide marked with a yellow star; **(c)** Eel River landslide inventory (Handwerger et al., 2019) (InSAR-derived only), shown in semi-transparent red; Eel River channel trace is shown with a blue line; the Boulder Creek landslide is marked with a yellow star.

2. Eel River

The Eel River watershed is located in northwestern California, a region with active tectonics, weak rocks, and high erosion rates where many geomorphic studies have been conducted before (e.g. Merritts and Bull, 1989; Kelsey, 1980; Brown and Ritter, 1971). Our study focuses on a section of the mainstem Eel River, at the junction with the Chamise Creek tributary (approximately 50 kilometers inland from the Mendocino County coast, south of Alderpoint) and spanning about 40 kilometers of the river extent in total (Figure 2b).

The Eel River basin contains basement rocks of the Central and Coastal belts of the Franciscan Complex mélange, containing tectonic blocks of Middle Jurassic, Cretaceous, and Paleogene graywacke, metagraywacke, blueschist, greenstone, chert, serpentinite, and minor amounts of limestone in a sheared matrix of argillite and graywacke (Clarke, 1992; Blake and Jones, 1981). Locally, our study area also has similar Broken Formation units to Big Sur. Its proximity to the Mendocino triple junction (MTJ) has made the formation of extensive shear zones and generally west trending synclinoria possible, further degrading the already weak mélange bedrock (Kelsey and Carver, 1988). Along the coast, tectonic uplift rates are variable but peak at ~5 mm/yr (Merritts and Bull, 1989; Merritts, 1996), but at our inland site, uplift rates are less than 1 mm/yr (Lock et al., 2006). This spatial gradient in uplift reflects the northward migration of the MTJ, which generates a wave of rock uplift and resultant base-level fall that propagates upstream through the Eel River network (Snyder et al., 2000; Foster and Kelsey, 2012; Willenbring et al., 2013).

Annual rainfall averages 1.4 m, falling primarily between October and May (Roering et al., 2015). The topography of the Eel River region is defined by the varying strengths of Franciscan mélange rocks. Harder sandstones form well-organized ridge and valley drainage networks, eroding primarily through fluvial processes, while the softer, fine-grained mélange has poorly developed drainage networks, low-gradient slopes, and erosion driven by earthflow movement (Mackey and Roering, 2011). Major axial drainages and ridges trend northwest (McLaughlin et al., 2000).

Despite having an order of magnitude lower rate of base-level lowering than Big Sur, the Eel River region still has high erosion rates relative to most of the California Coast Ranges (Roering et al., 2015). In the 1960's, the Eel River had an annual sediment yield approaching 4000 tons per square kilometer, higher than any other non-glacial, continental river in the United States (Brown and Ritter, 1971). Modern erosion-rate estimates agree with this pattern: cosmogenic radionuclide-derived rates from nearby subcatchments (including Redwood Creek, the upper Van Duzen River, and the South and main-stem Eel River) range from ~0.14-1.1 mm/yr (Ferrier et al., 2005; Fuller et al., 2009; Balco et al., 2013; Willenbring et al., 2013). These data support our decision to study the Eel River region's landslide-driven patterns of landscape change in response to base-level lowering. Despite erosion rates that exceed those of most other North American river systems, slow-moving earthflows remain the dominant landslide style here. Rather than releasing all at once as a discrete failure, an earthflow persists as a slowly creeping mass for decades to centuries, advancing in a manner more akin to glacial-style creep than to a "conventional" landslide's single mobilization event. A defining characteristic of Eel River landslides is their strong seasonal behavior; earthflows speed up during the wet season and slow again through the dry months as pore fluid pressures rise and fall (e.g. Iverson and Major, 1986; Bennett et al., 2016; Handwerger et al., 2022). InSAR studies further show that entire landslide bodies can move synchronously during wet periods, indicating hydrologic coupling throughout the slide mass (Handwerger et al., 2015).

METHODS

To identify the mechanisms driving the transition between earthflow and rotational landslide activity within Franciscan mélange, we pair detailed topographic mapping and analysis of landslide inventories with two-dimensional numerical slope stability modeling. Landslide mapping allows us to characterize how failure style and morphology vary systematically between our two field sites, while our numerical experiments let us test which combinations of material properties and erosional boundary conditions can reproduce these observed patterns.

Mapping

1. Big Sur

Although significant effort has gone into characterizing landslides along the central California coast (Wills et al., 2001), they do not extend beyond the Highway 1 corridor and were mapped before the advent of high-resolution lidar imagery. As part of this study, we created a lidar-derived landslide inventory of our study watersheds in Big Sur to explore how geologic context and a fuller landslide history may inform future hazard potentials across Big Sur. We used 1-m resolution USGS 3DEP LiDAR-derived hillshades (USGS, 2024; "CA_AZ_FEMA_R9_Lidar_2017_D18") to map landslides within three large drainage basins (Willow Creek, Alder Creek, and Villa Creek; Figure 2b) to evaluate how landslide morphology and process differs along a gradient from the coast to the ridge-tops.

Landslide mapping approaches vary widely depending on data resolution and the clarity of diagnostic surface features, which is a particular challenge in Franciscan mélange terrain where the material's inherently uncohesive nature often obscures the discrete traits that typically distinguish a landslide in map view (like an abrupt break in slope clearly corresponding to a singular deposit, an obvious transition in surface roughness, and/or an unincised deposit). Because our goal was to relate the spatial distribution of Big Sur's landslides to their present-day kinematics, we used DOGAMI's landslide mapping protocol (Schulz, 2004a; Baum et al., 2005; Burns and Madin, 2009) as a starting point and adapted it to address these site-specific challenges. To map these more diffuse surface signatures, we identified signs of slope failure in the spacing of topographic contours (a transition from concave head scarp to convex toe) and in qualitative assessments of the terrain's roughness, patterns of surface fracturing (tension and transverse cracks) and deformation, and relative proximity to other mapped landslides and to the coast. Satellite imagery supplemented our high-resolution lidar data, helping identify locations where large-scale (>10,000 m²) landslide events had disturbed vegetation cover or exposed underlying bedrock, though dense forest across lower-elevation portions of the study area limited visibility across much of the terrain. In general, we identified the head scarp of a given landslide by locating areas of pronounced shadowing on the hillshade consistent with steep, slope-facing terrain, then used the head scarp polygon as a guide for mapping the corresponding deposit (Figure 3). Given that hillshade has a strong directional bias, we also layered a slope raster, as well as 1m and 3m topographic contours on top to make steeper terrain contrast well against shallower terrain.

After mapping the entire study area, we conducted several rounds of review and editing to improve accuracy. For each landslide, we verified that all vertices along shared polygon edges were properly snapped together, confirmed that any overlapping polygons represented geomorphically plausible relationships (like nested or superimposed failures), and checked for topological errors such as unfilled gaps, sliver polygons, or duplicate vertices. This review process was repeated iteratively throughout mapping to ensure accuracy and internal consistency.

2. Eel River

Our inventory of active earthflows in the Eel River came from four primary sources: Mackey and Roering (2011), Handwerger et al. (2015), Bennett et al. (2016), and Handwerger et al. (2019). Mackey and Roering (2011) mapped earthflow activity by tracking the displacement of trees and shrubs visible in airborne lidar and aerial photographs from 1944 to 2006, while Bennett et al. (2016) mapped active earthflows from Google Earth™ imagery from 1988-2014.

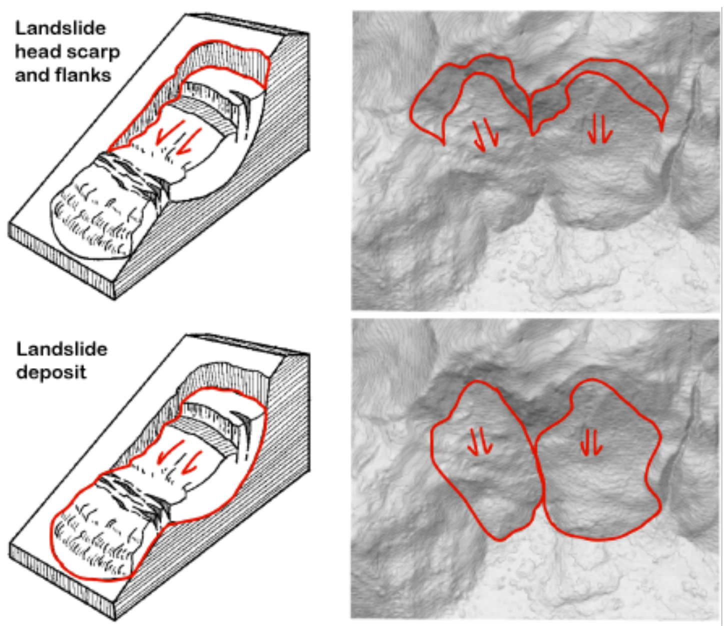

Figure 3: Adapted from Burns and Madin (2009); The two types of spatial data we compiled while mapping Big Sur's landslides.

Handwerger et al. (2015, 2019) mapped active earthflows in this region by coupling the lidar DEM with InSAR data, though the two studies draw on different InSAR platforms and time periods. Handwerger et al. (2015) used InSAR data from the satellite-based ALOS-1 platform (launched in early 2006, with repeat coverage of the Eel River at roughly 1.5-month intervals), drawing on scenes collected between February 2007 and January 2011. Handwerger et al. (2019), by contrast, used airborne UAVSAR data focused specifically on the Boulder Creek landslide (the largest landslide in the Eel River study area, Figure 2c) collected between 2015 and 2017. The lidar DEM underlying both studies comes from an NCALM (National Center for Airborne Laser Mapping) mission flown in 2006, which acquired a 200 km^2 airborne lidar dataset processed to 1 m spacing along a section of the Eel River encompassing the Boulder Creek earthflow (Roering et al., 2009). We accessed this same DEM via OpenTopography.org and used it to underpin our analysis of mapped earthflows along the Eel River.

Because Handwerger et al. (2015) and (2019) relied on InSAR coverage from different platforms, time periods, and spatial extents, the resulting earthflow inventory is necessarily a composite of landslides that were actively deforming during different, only partially overlapping windows of observation. This distinction matters because, unlike the Big Sur landslide inventory, which includes both active and inactive landslides, the Eel River inventory consists only of landslides identified as active during these specific InSAR observation periods. As a result, despite covering a larger area, the Eel River inventory contains substantially fewer mapped landslide polygons than Big Sur (275 in the Eel River versus 1402 in Big Sur), which makes a direct, “apples-to-apples” comparison between the two sites more difficult. We therefore proceed under the assumption that the actively deforming landslide population captured in our database is broadly representative of the total landslide population in the region, though we acknowledge this assumption cannot be fully verified with the data available.

Finally, the Eel River landslide polygons required an important pre-processing step before further analysis. Certain earthflow complexes (defined as multiple shallow movements showing evidence of intersecting/overlapping flow paths) were originally mapped as large individual polygons with multiple "arms" protruding from the main slide body. This posed a particular problem for our aspect ratio analysis (discussed in section 3.2), because a simple bounding-box calculation of aspect ratio would be skewed by the arms increasing the overall width of the polygons. To resolve this, we first separated the original, merged earthflow complex polygons (Figure 4a) into their individual smaller earthflow components (Figure 4b). This way, each shallow movement is quantified by its own geometry, rather than by the geometry of the larger complex it contributes to. Lastly, we developed a Python workflow for more accurately calculating the width and length dimensions of the more geometrically complex (i.e. curving with changes in topography) earthflow polygons, which is discussed in more detail in the next section.

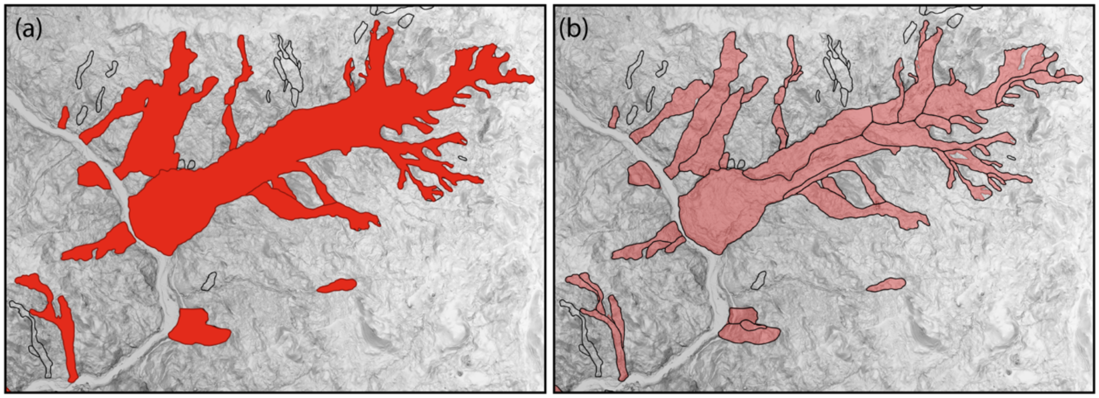

Figure 4: Breaking up earthflow complexes in Eel River into their constituent slides; **(a)** the original Boulder Creek landslide polygon, mapped from InSAR as one singular polygon; **(b)** the Boulder Creek landslide decomposed into more than 20 individual earthflows.

Topographic Analysis

Landslide morphology is a fundamental indicator of deformation style (Varnes, 1978; Hungr et al., 2014). Here we conduct an analysis of landslide slope and aspect ratio, or the ratio of its downslope length to its cross-slope width. A landslide with a high aspect ratio would be very long and very narrow, as opposed to one with an aspect ratio closer to 1 which would have relatively similar length and width measurements. This parameter can be used to classify mapped landslides as earthflows or rotational landslides, since earthflows typically have a long, narrow shape and therefore a high aspect ratio (Hungr et al., 2014; Figure 5b), whereas rotational landslides have smaller aspect ratios (e.g., Martel, 2004; Figure 5a).

With simpler, rectangular geometries, aspect ratio is easily calculated by dividing the length of the polygon by its width. However, the landslide polygons we work with (particularly the ones in the Eel River region) have much more elaborate geometries with curves, corners, and multiple lobes, reflecting the complexity of Francican mélange topography. To calculate a meaningful aspect ratio for these irregular polygons, we first determined a downslope direction unique to each landslide by fitting a best-fit plane to the elevation values within its footprint (via linear regression) and taking the direction of steepest descent as that polygon's downslope azimuth. Having the aspect ratio measurement be oriented in the downslope direction was an important step for distinguishing long, narrow earthflows from short (i.e. low relief) and very wide rotational landslides. We then projected the polygon's vertices onto this downslope axis and its corresponding cross-slope axis and calculated the difference between the maximum and minimum projected values to represent its length and width respectively. Aspect ratio was then calculated as the ratio of downslope length to cross-slope width. This same methodology was also used to calculate the dimensions of the Big Sur landslide polygons.

The slope of the polygon was calculated by extracting a slope raster from the DEM in QGIS and taking the average of the slope values ascribed to each pixel within a landslide polygon. Given that earthflows typically occur on shallower slopes (Figure 5d) while rotational landslides tend to occur on steeper slopes (Figure 5c), measurements of average slope paired with observed aspect ratio can be highly effective for classifying landslide type based on morphology. Landslide relief was calculated simply by subtracting the maximum elevation of a polygon from the minimum, and we extracted two-dimensional area values for each landslide polygon. Importantly, these measurements were taken on the Big Sur landslides' deposit polygons, since the Eel River slides were mapped without head scarp polygons. These morphometric parameters were necessary for us to gauge the variance in landslide topology and therefore process at a broader field scale.

Our final topographic analysis step was a comparison of the morphology of landslides in Big Sur and Eel River and their proximity to the base-level control (in Big Sur, the coast; in Eel River, the main river channel). We used Euclidean distances to make this comparison, which were extracted in QGIS by connecting a line from the centroid of each landslide polygon to the closest point on a line tracing either the coastline or the river channel. The lengths of these lines were saved as attributes of their corresponding landslide, which were then compared to its other attribute values of slope, aspect ratio, and area.

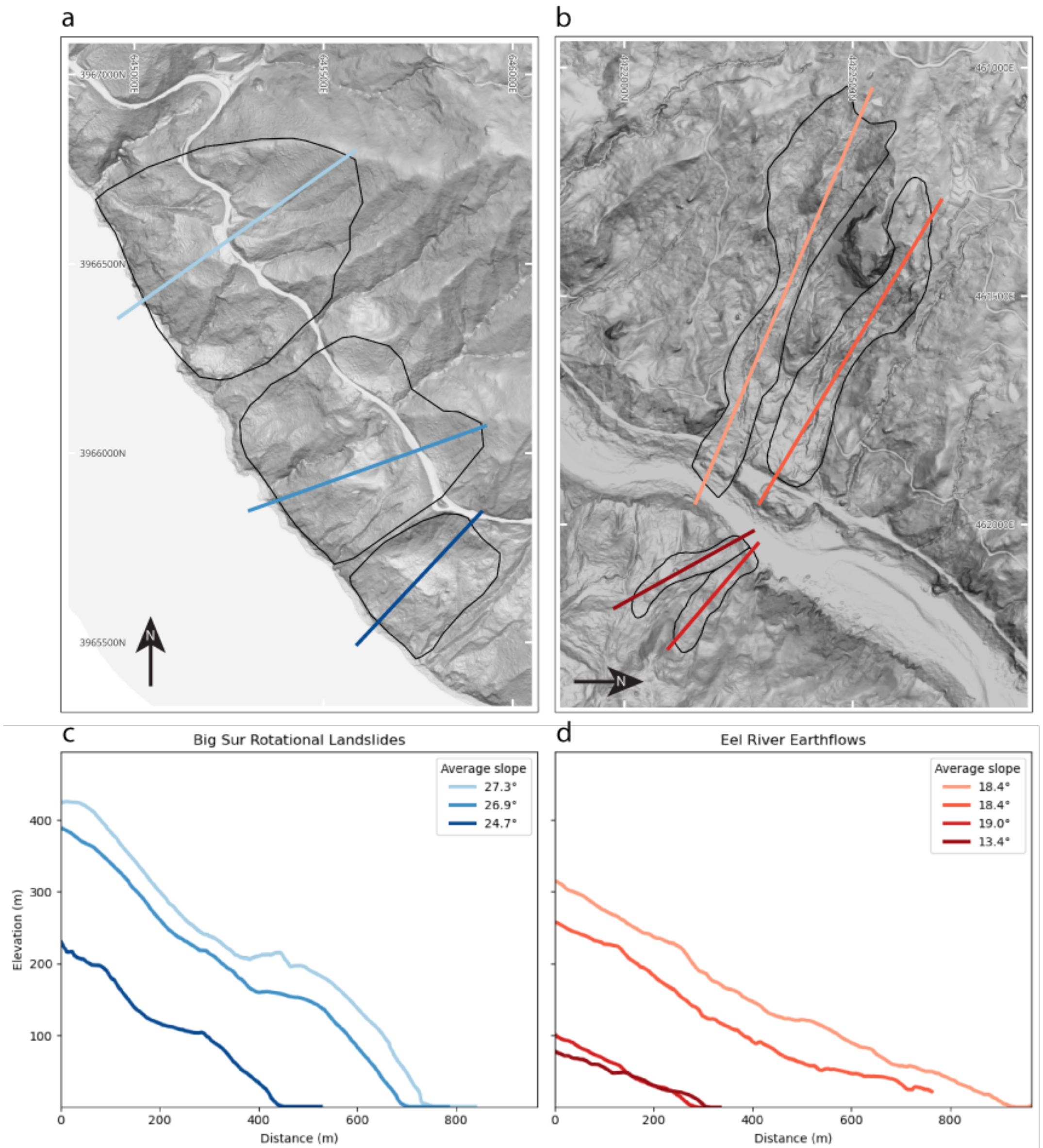

Figure 5: Downslope elevation profiles of high-aspect-ratio rotational landslides in Big Sur **(a, c)** and low-aspect-ratio earthflows along the Eel River **(b, d)**, showing the link between landslide aspect ratio, average slope, and process/type.

2D Numerical Modeling

We used RocScience's RS2 slope stability software to evaluate the impact of lateral erosion on landslide size and style. RS2 uses the Finite Element Method (FEM) to quantitatively assess slope stability by solving the stresses and deformations for an elasto-plastic material using a triangular or quadrilateral mesh. For each test case, we ran the model to a converged equilibrium solution using the input strength values for the uniform and layered strength scenarios described below (Table 1) and evaluated the resulting patterns of strain and displacement. Because we are interested in the hillslope's response to progressive toe erosion over geomorphic time rather than in resolving a single complete failure sequence, we do not incrementally weaken the material to model a discrete failure event at each time step. Instead, we treat topographic change between successive test cases as the primary mechanism used to induce progressive failure in the model.

We simulated two hypothetical hillslope strength distributions: (1) a uniformly weak mélange lithology, and (2) a layered model with a thin (~10 m) layer of weak mélange overlying a strong mélange lithology at depth. For the layered model, we used a mesh that coarsens with depth, providing higher resolution near the weathered layer where stress gradients are expected to be greatest. Additionally, we used a standard weathered zone thickness of 10 m. We derived this number using Eel River earthflow toe depth measurements from Mackey and Roering (2011), which averaged to about 12.7 m, which was rounded down to 10 m for the sake of simplicity.

For the layered scenario, we modeled three hillslope configurations T1-T3. In the first test case (T1), we used a continuous 20º hillslope (550 m wide and 230 m tall with 100 m wide flats on either side), representing the initial, pre-incision condition. The next test case (T2) used the same 20º hillslope but with 100 m of lateral incision (19% of the total width of the hillslope), producing a 40º break in slope. The third test case (T3) increased total lateral incision to 200 m (38% of total width), retaining the same 20º-to-40º break in slope as T2 and yielding a higher-relief coastal bluff. For the uniform scenario, we modeled only the first two configurations (T1 and T2). Based on the amplified but qualitatively unchanged failure pattern observed between T1 and T2 (discussed in section 4.2), we inferred that additional toe material removal would be unlikely to meaningfully alter this result and did not run a T3 case. Across all test cases, we did not incorporate groundwater effects, given the lack of site-specific subsurface groundwater data, and applied gravitational loading as the only loading condition in the model.

	Weak Mélange	*Strong Mélange*
Unit Weight (kN/m³)	19	21
Poisson's Ratio	0.3	0.3
Young's Modulus (kPa)	100,000	500,000
Failure Criterion	Mohr-Coulomb	
Material Type	Plastic	
Peak Tensile Strength (kPa)	50	200
Peak Friction Angle (º)	18	30
Peak Cohesion (kPa)	10	50

Table 1: Material properties of modeled mélange lithologies

RESULTS

Big Sur Mapping and Topographic Analysis

Our Big Sur landslide inventory has over 1400 individually mapped landslides (Figure 2a). The three mapped watersheds have an average landslide density of about 18 landslides per square kilometer, covering roughly 33% of the total map area. Along the coast, landslides are larger in area and show complex overlapping relationships, indicating large (>10,000 m^2) initial failures followed by reactivations within the original landslide deposit and in adjacent material (Figure 2a). Farther inland, landslides form fewer complexes and become smaller and more uniform in size and shape. Nearly all active landslides are part of larger complexes within the high-relief (300-600 m) coastal zone (Figure 6). Overall, we find that many of the active landslides along the southern Big Sur coast exhibit complicated, multi-generational histories, potentially linked to the landslides' proximity to the coast, discussed later in this section.

To translate this variation in aspect ratio into an explicit classification scheme, we use the distribution of aspect ratio and mean deposit slope across both study areas (Figure 6c) to identify characteristic morphometric signatures for each failure style. Big Sur landslides cluster around a mean aspect ratio of 1.15 and a mean slope of 30.7º, consistent with compact, equant geometry expected of rotational failure, whereas Eel River landslides cluster around a mean aspect ratio of 2.30 and a mean slope of 20.4º, consistent with the elongated geometry characteristic of earthflows.

These two populations overlap substantially in aspect ratio space (roughly 1.5-2.0), reflecting a continuous morphological gradient rather than a sharp boundary between failure styles. Given this, we adopt an aspect ratio of ~1.7 as a working threshold for morphology-based classification in this study, with landslides below this value classified as consistent with rotational failure and those above as consistent with earthflow behavior. Individual landslides near the boundary are best interpreted as morphologically transitional rather than confidently assigned to either failure mode. Notably, when we examine the subset of Big Sur landslides independently confirmed to be currently active via UAVSAR (Figure 6a and 6c), most fall within the low-aspect ratio, rotational-consistent range, but a small number extend to aspect ratios above our proposed threshold, indicating that earthflow-like morphology, while comparatively rare, is not entirely absent from Big Sur's actively deforming population.

Given that active landslides in Big Sur are concentrated near the coast (Figure 6a), we hypothesized that landslide morphology might vary systematically with proximity to the coast or river channel. To test this, we compared each landslide's Euclidean distance to the coast or river channel against its slope and aspect ratio. Landslide slopes in Big Sur are consistently ~10º higher than the landslides' slopes in the Eel River area, but neither area has substantially variable slope values within the population, regardless of distance from the primary erosional agent (Figure 7a). Similarly, landslide aspect ratios in Big Sur are consistently lower than those found in the Eel River area, but there is still no strong correlation between aspect ratio value and distance from the coast or river channel (Figure 7b). Finally, we were able to observe Big Sur landslides' areas increasing with proximity to the coast, concluding in a sharp drop at the coastline itself (Figure 7c), reflecting how the coastal bluffs host less-frequent large area failures with many smaller internal reactivation events and minor secondary collapses associated with the direct impact of wave action. Meanwhile, the Eel River landslides' areas, despite being an order of magnitude larger than the ones we find in Big Sur, do not correlate strongly with distance to the river channel. Taken together, these results offer some evidence that distance from the primary erosional agent may modulate landslide morphology (most notably through the trends observed in Big Sur landslides' areas) but the relationship is too inconsistent across slope, aspect ratio, and area to allow for any definitive interpretation of proximity as a controlling factor.

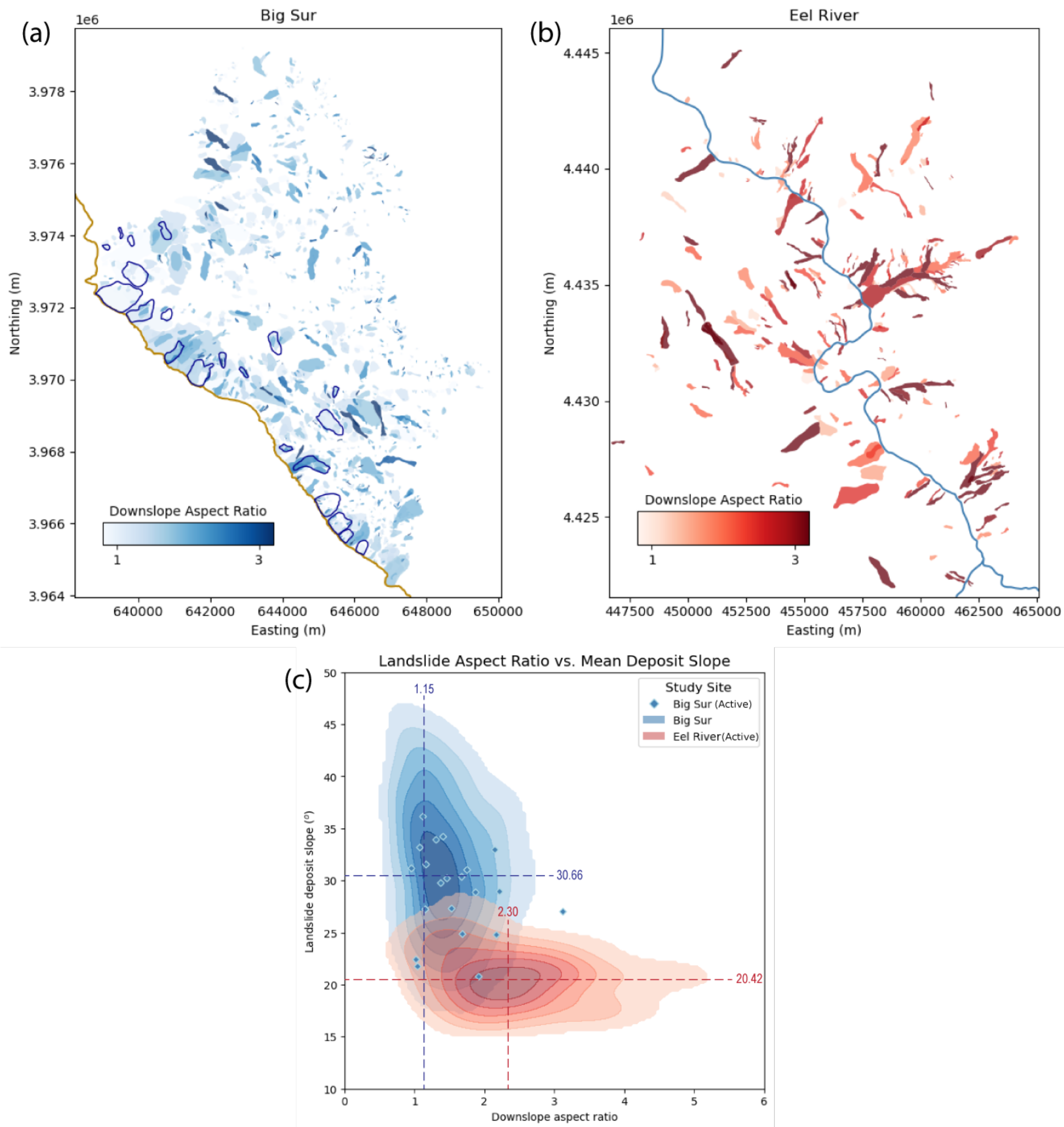

Figure 6: (a) downslope aspect ratio of landslides in Big Sur, **(b)** downslope aspect ratio of landslides in Eel River, **(c)** downslope aspect ratio of landslides plotted against mean deposit slope in each study area. Blue and red dashed lines show average landslide deposit slope and downslope aspect ratio values for each locale. Blue outlined landslides in (a) are active as derived by InSAR mapping (Winter et al., 2024) and are represented in (c) as blue diamonds. The gold line in (a) and blue line in (b) represent the coastline and river channel, respectively. Distribution in (c) is represented as a contour cloud since the Big Sur dataset has more than four times as many data points than the Eel River dataset and includes both active and inactive landslides while the Eel River data set includes only active landslides.

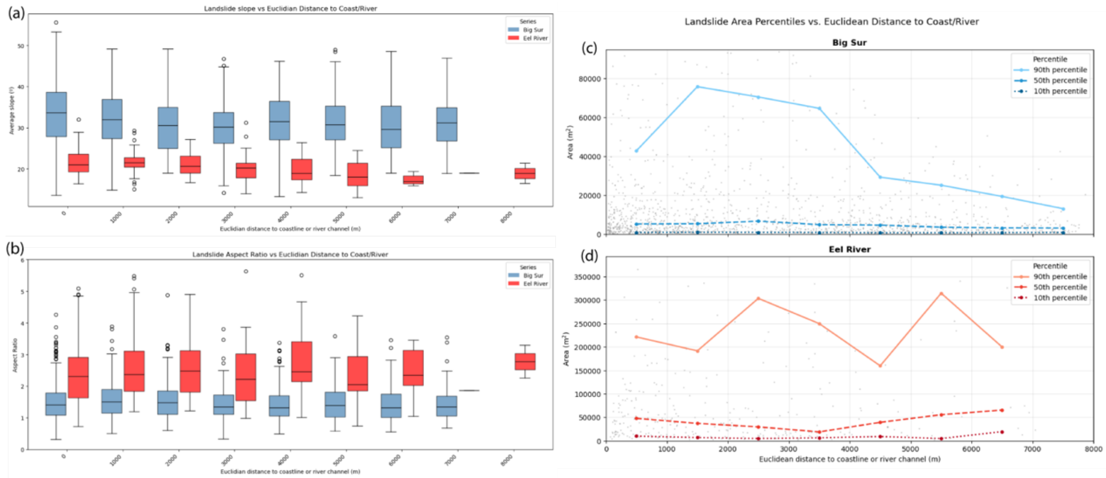

Figure 7: Euclidean distance plotted against slope **(a)** and aspect ratio **(b)** for the Big Sur and Eel River inventories (shown in blues and reds, respectively). **(c)** and **(d)** show Euclidean distance plotted against landslide area for Big Sur and Eel River respectively, but since the two populations had area measurements in different orders of magnitude, we opted to present the data as line plots of the 90th, 50th, and 10th percentile values, with individual data points shown in light gray. Also, note the scale differences in the vertical axes of (c) and (d).

2D Modeling of Landslide Process Transition Across Landscape Configurations

Our modeling results show distinct differences in landslide size and style depending on lithologic configuration. For the uniform lithology experiment (Figure 8a), T1 shows that a 20-degree slope in homogeneously weak mélange produces a deep seated, curved zone of high strain, indicative of a rotational failure. However, the deformation is broad and diffuse, extending deep into the slope interior, indicating a wide, distributed zone of internal shearing rather than a localized failure surface. This observed zone of deformation is typical of what will eventually nucleate into a defined slip surface, if we were to observe the full progressive failure sequence in RS2 (here we only observe a single step of that progression). With erosional debuttressing at the landslide toe in T2, this same pattern is amplified with displacement increasing at the base of the slope. Because this progression showed no qualitative change in failure style between T1 and T2, we did not run a third test case with further erosion for the uniform lithology scenario, reasoning that additional toe material removal would be unlikely to produce a significantly different result.

For our layered lithology experiment (Figure 8b), T1 shows that only the shallow weak layer mobilizes under gravitational loading, reproducing motion typical of earthflows. After removing 100 m of material at the hillslope toe in T2, the weak layer again mobilizes, but a subtle zone of rotational strain also begins to form in the underlying strong mélange. Finally, after removing a further 100 m of toe material in T3 (200 m total) resulting in a higher-relief coastal bluff, the model develops a clear, deep-seated rotational failure surface beneath the mobilized surface layer. Across this T1-to-T3 progression, the layered lithology scenario reproduces the process transition from slow-moving earthflow to fast-moving rotational landslide via progressive toe erosion. In contrast, this transition could not be reproduced in the uniform lithology scenario under any tested boundary condition.

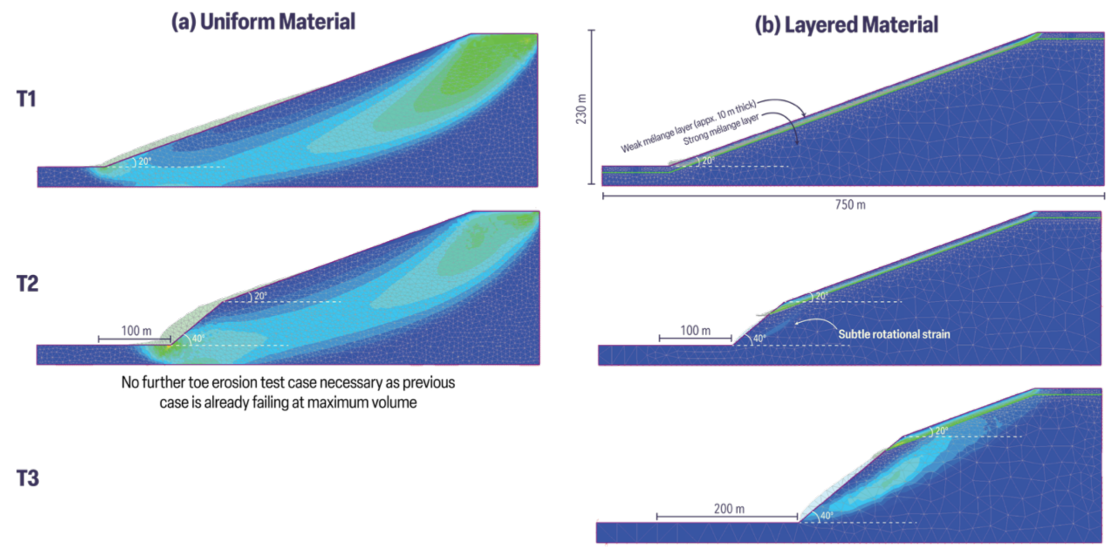

Figure 8: Results of RS2 numerical modeling showing strain/displacement contours (green = highest strain) in **(a)** a slope made of a single homogeneous material with a uniform mesh and **(b)** a slope with a thin (~10 m thick) weak mélange layer overlying a strong mélange unit with a graded (fining upwards) mesh.

DISCUSSION

Base-level lowering and landslide style

The results of our mapping in Big Sur and along the Eel River demonstrate two related patterns: (1) large, active landslides in Big Sur are concentrated along the coast where wave action drives rapid base-level lowering, and (2) Big Sur's landscape is dominated by landslides with morphologies consistent with rotational landslides while Eel River's landscape is dominated by landslides with morphologies consistent with slow-moving earthflows (despite being situated in the same Franciscan complex mélange lithology). Together, these patterns point to a relationship between landslide failure style and overall hillslope gradient, one that in our two study regions appears to be set by contrasting rates and styles of base-level lowering.

Big Sur experiences rates of coastal erosion at an average rate of about 2 cm per year driven by wave action (Dow et al., 2026). Because this erosion removes material laterally rather than vertically, we can express it as an equivalent vertical base-level lowering rate by accounting for local hillslope geometry. For a hillslope of about 45º (comparable to the steep coastal slopes found in Big Sur) a lateral erosion rate of 2 cm/yr corresponds to a vertical lowering rate of a similar magnitude, since tan(45º) = 1. This rate of coastal erosion is roughly an order of magnitude higher than the rate of base-level lowering of the Eel River (~1 mm per year) driven by river channel incision (Willenbring et al., 2013; Bennett et al., 2016; Roering et al., 2015). Our results show that in both sites, earthflows form on shallow slopes of about 15-20º. However, the steepest areas of Big Sur, with slope angles above 30-40º, are where nearly all active landslide motion occurs.

It is well-established that rising groundwater saturation can trigger landslides by increasing pore-fluid pressure and reducing the effective stress holding a slope together (Iverson, 2000). We apply the inverse of this logic to our hypothesis; by increasing the rate of vertical incision at a hillslope's base, base-level lowering can promote more efficient groundwater drainage, thereby reducing pore-fluid pressure near the ground surface and acting to suppress the shallow, saturation-driven earthflow motion that would otherwise dominate. This suggests that the order-of-magnitude difference in base-level lowering rates between our two field sites should produce two distinct hillslope responses, which we describe below.

1. Eel River Response

We speculate that along the Eel River, the rate of vertical incision is slow enough that hillslopes can reach a critical slope angle and water saturation level gradually. Once this threshold is crossed, earthflows will activate and transport material downslope (e.g. Finnegan et al., 2021; Murphy et al., 2022; Iverson and Major, 1986), which effectively maintains the region's characteristically shallow hillslope angles (Figure 9a). This saturation dependence is consistent with observations that the water table in active earthflows typically sits at or near the ground surface (Iverson and Major, 1986), sustaining the elevated pore-fluid pressures needed to keep the sliding mass mobilized. This self-limiting behavior is reinforced by the mechanics of earthflow motion itself. Persistent earthflow activity is typified by rate-strengthening behavior (Finnegan and Saffer, 2024), a frictional response in which resistance to sliding increases as slip accelerates, acting as a natural brake against runaway failure. In this way, persistent earthflow activity can help maintain the shallow gradients required for its own initiation, preventing the slow-to-fast transitions that we have observed in Big Sur.

Earthflows likely also reinforce this stability through their role in long-term erosion. Booth and Roering (2011) show that earthflow activity substantially lowers land surface elevation on the upper portions of hillslopes while delivering an approximately steady flux of sediment to the middle and lower portions of hillslopes, a process they quantify using a non-Newtonian flow rheology model of long-term sediment transport. Put another way, earthflows function as a continuous, moderating release valve for hillslope material, rather than allowing stress and relief to build towards a more catastrophic failure. Indeed, this mechanism would not be contributing significantly to landscape evolution in Big Sur where active earthflows are comparatively rare.

This picture of long-term kinematic stability is further supported by direct evidence. Handwerger et al. (2015) compared 13 Eel River landslides to Mackey and Roering's (2011) earlier landslide inventory and found that the locations of the earthflows' kinematic zones have remained fixed for almost 70 years, strongly suggesting that landslide geometry, once established, exerts a primary control on long-term kinematic behavior. Along the Eel River, this geometric persistence likely contributes to earthflows' continued dominance as the region's primary landslide style.

2. Big Sur Response

In Big Sur, we posit that as coastal bluffs steepen beyond a critical slope angle threshold, they lose the capacity for the shallow surface deformation that characterizes earthflows and instead fail deeper in the bedrock in a rotational landslide (Figure 9b). Leshchinsky et al. (2019) examine this same possibility in the Oregon Coast Range, showing that the rate of landslide advance is highly sensitive to changes in erosion rate. This may have a disproportionate effect on landslides with low aspect ratios like those we observe in Big Sur, where the removal of buttressing material at the toe is proportionally more destabilizing than for more elongate failures. This sensitivity appears amplified by the local lithology; Hapke and Green (2006) find that material removal along steep, high-relief coastal slopes in Big Sur occurs up to six times faster in weak Franciscan mélange than in the regions Cretaceous and Tertiary sedimentary rocks.

Further, we propose that the processes capable of relaxing an over-steepened hillslope (earthflow activity, hillslope diffusion, and other forms of gradual mass transport) are simply not fast enough to keep pace with a coastline retreating at rates an order of magnitude higher than the Eel River's vertical incision rate. Rather than the hillslope gradually lowering its overall gradient through earthflow-style creep like we see along the Eel River, the toes of the Big Sur hillslopes are repeatedly removed faster than the slope above it can relax in response, so the slope keeps getting steeper instead of settling into a new stable form.

This dynamic offers a plausible explanation for why Big Sur's catastrophic failures can be preceded by years of slow deformation. As mentioned previously, Mud Creek itself did not activate suddenly in 2017; it had been creeping for about eight years prior (e.g. Warrick et al., 2019). This progression is consistent with our broader hypothesis regarding weathering and base-level. Because the thickness of a hillslope's weathered layer governs both water table depth and the amount of stress that can accumulate above a potential failure plane before saturation reaches the surface (Murphy et al., 2022), a hillslope experiencing progressive toe material removal may initially continue to behave like a shallow, earthflow-prone feature even as the underlying geometry is destabilized. Slow deformation can therefore persist for years while coastal retreat works to remove buttressing material and expose comparatively unweathered rock at depth. Once the accumulated stress and steepened geometry can no longer be accommodated by shallow creep, the hillslope will fail catastrophically and at depth. Together, these lines of reasoning point to Big Sur's rapid, order-of-magnitude-elevated base-level lowering rate as a plausible driver not just of steeper average hillslope gradients, but of a fundamentally different landslide process altogether: one in which outwardly modest surface creep may mask a hillslope's slow transition toward catastrophic failure.

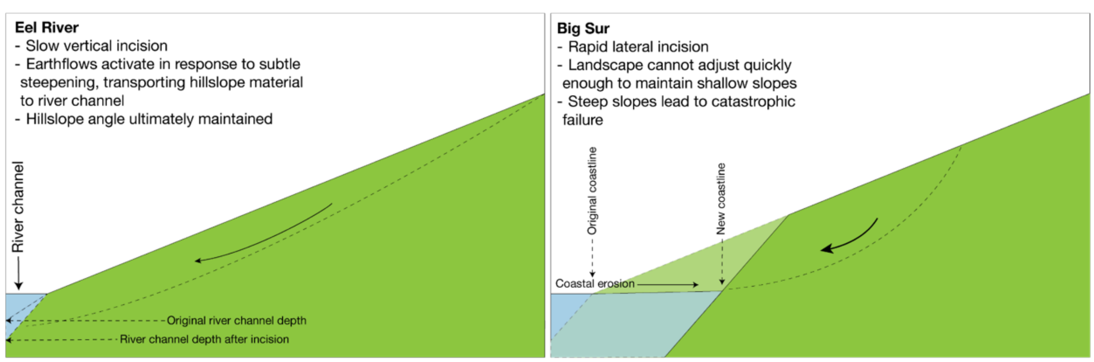

Figure 9: Schematic diagram showing how the large difference in base-level lowering rates in Big Sur and Eel River might result in the higher or lower hillslope angles needed for either rotational landslides or earthflows to dominate in each landscape.

Numerical Modeling

Our numerical modeling experiments help explain why differing rates of the base-level lowering process produce such different landslide morphologies in our two field sites and point to lithologic layering as an additional necessary ingredient for earthflow activity. In our uniform material experiment (Figure 8a), our results showed that a slope composed of homogeneously weak mélange materials cannot produce earthflow-like motion under any of our tested boundary conditions. However, our layered material experiment (Figure 8b) was able to capture the process transition we hypothesize is occurring in Big Sur, suggesting that some degree of vertical heterogeneity may be a prerequisite for sustained earthflow behavior.

1. The role of weathering in the layered material experiment

Such vertical gradients in rock strength within mélange have been explored in the context of studies of rock weathering and critical zone processes. For example, Hahm et al. (2019) argue that the transition from weathered to unweathered bedrock in mélange (typically about 3 m below the surface) is controlled by the depth to which seasonal drainage of the vadose zone occurs. Perennially saturated mélange has much lower hydraulic conductivity than its seasonally drained counterpart. Murphy et al. (2022), in turn, show that the shallow depth of the water table in mélange means that earthflows have little capacity to increase their pore fluid pressure. This has significant implications for the rate of landslide motion and overall failure style, since the thickness of the unsaturated zone (i.e. the area above the water table) also controls the depth of a landslide's failure plane. Further, Murphy et al. (2022) states that landslides formed in settings with thicker subsurface weathering zones may have the potential to build up significantly more stress above the failure plane before the water table reaches the surface, resulting in a catastrophic failure. With this basis in mind, we hypothesized that in areas with a sufficiently thick weathered layer and higher rates of wave-driven coastal erosion, stronger unweathered rock would eventually become exposed along the coast, making it possible to maintain the steeper hillslope angles necessary to trigger a catastrophic slope failure like the ones we see in Big Sur.

Overall, the results of the layered experiment sufficiently capture the process transition we expected to see after progressively removing hillslope toe material. In T1, gravitational loading alone is sufficient to mobilize the shallow weathered layer, reproducing the shallow detachments that are characteristic of earthflows in settings like the Eel River region. This suggests that where the rate of weathering is fast relative to the rate of base-level lowering at the landslide toe, hillslopes can accommodate incision through continuous, shallow deformation. The intermediate stage in T2, marked by the low-level formation of a deep-seated rotational failure plane, indicates that as the rate of base-level lowering begins to outpace the rate of weathering, the failure plane begins to migrate downward into stronger, less-weathered material. This implies a mechanical transition in how the slope accommodates stress; rather than deforming plastically near the surface, the hillslope begins to store elastic strain at depth. By T3, this process culminates in the complete development of a deep-seated failure plane, showing that the hillslope that was previously only capable of shallow, slow-moving deformation has apparently become capable of failing at depth in large rotational failures that have potential for catastrophic acceleration. Together, these stages show that the earthflow to rotational failure transition observed in Big Sur may be driven by coastal erosion outpacing the rate of weathering, exposing the stronger underlying rock before it can weather to the point of accommodating shallow creep again, effectively forcing the hillslope towards deeper, and potentially more catastrophic failure modes.

Regarding the uniform material experiment's failure to reproduce earthflow-like motion, we acknowledge that the model only samples the hillslope's response to two discrete, large-magnitude toe-removal events, whereas earthflows in the field typically evolve in response to progressive, incremental erosion sustained over years or decades. This is a limitation of the current experimental design, and future modeling work should test whether a more gradual, continuously applied erosion boundary condition might permit some degree of stress redistribution within the hillslope. Until then, we cannot fully rule out the use of a uniform hillslope model to reproduce the process transition based on the two-step approach used here.

Potential Sources of Error and Paths for Continued Study

A key limitation of this our numerical modeling analysis is that it treats the Franciscan mélange as texturally homogeneous, when its defining characteristic is the opposite: a block-in-matrix texture in which competent blocks of greywacke, chert, and greenstone are suspended within a weak, sheared clay matrix (e.g. Medley, 2001; Kim et al., 2004; Lindquist and Goodman, 1994), and the two constituents differ dramatically in shear strength. This simplification is standard practice for finite element models like RS2, but it means our results cannot capture how block size, shape, or volumetric concentration might locally alter stress distribution, and thus failure geometry. Future modeling efforts could address this by incorporating discrete block geometries directly into the mesh, or by using equivalent strength parameters informed by field-constrained block proportions.

While our modeling suggests that vertical strength heterogeneity is necessary to reproduce the landslide process transition observed in Big Sur, the specific thickness of the weathered layer used in our layered model (Figure 8b) remains approximated rather than field-constrained. Seismic refraction surveying offers a means to directly test and refine this assumption. Seismic refraction surveys are routinely used to image weathering depth profiles (e.g. Huang et al., 2021) and would effectively delineate the boundary between weathered and unweathered material. Carrying out refraction surveys at both Big Sur and the Eel River region would offer a valuable test of our broader hypothesis regarding the role of coastal erosion in exposing stronger materials and would also allow us to move toward a more quantitative assessment of whether the weathered layer thickness varies between erosion regimes in the way our modeling results imply. Overall, pairing seismic refraction data with our numerical framework would allow future experimental models to be initialized with site-specific, geophysically constrained layer geometries rather than idealized end-member cases. With these additional data, it might be possible to discern whether vertical strength heterogeneity is not only necessary but sufficient to explain the differences in landslide morphology and process transitions observed in the field.

CONCLUSION

This study set out to explain a contrast within a single, notoriously weak rock unit: why the Franciscan mélange produces slow-moving earthflows in some settings but is apparently capable of collapsing in a rotational landslide in others. By combining landslide mapping, morphometric analysis, and two-dimensional numerical modeling, we show that this contrast is not an inherent property of the mélange itself, but a consequence of the rate and style of base-level lowering acting on it.

Our landslide inventories show that Big Sur's actively deforming landslides are concentrated along its rapidly eroding coastline and are dominated by compact, low-aspect ratio morphologies consistent with rotational failure, while the Eel River's active landslides are dominated by elongate, high-aspect-ratio morphologies consistent with earthflow motion, despite both regions sharing the same parent lithology. Our numerical modeling results show that this process transition can be reproduced under progressive erosion of a hillslope's toe material, but only within a hillslope containing vertical strength heterogeneity from a weak weathered surface layer overlying a stronger, unweathered mélange at depth. An equivalent, uniform-strength hillslope never produces this transition, regardless of how much toe material is removed. Together, these results show that the transition from earthflow-dominant to rotational-landslide-dominant terrain within Franciscan mélange is likely governed by the interaction between base-level lowering rate and the rate of development of the weathering layer, rather than by lithology alone.

These findings carry meaningful implications for how landslide hazard is assessed in Franciscan mélange terrain, and in rapidly eroding coastal settings more broadly. Slow, distributed earthflow motion is rarely perceived as hazardous, especially in comparison to abrupt, catastrophic failure. Our results complicate that assumption because they suggest that a hillslope experiencing sustained, rapid base-level lowering may be gradually transitioning toward far more dangerous rotational failure, even when the surface shows only modest deformation. This is a particularly urgent concern for coastal communities and infrastructure situated near actively retreating coastlines like Big Sur’s.

Ultimately, this work demonstrates that landslide hazard in weak, sheared rock like the Franciscan mélange cannot be assessed based on lithology alone. Hazard is instead a culmination of the hillslope’s erosional boundary conditions and its internal structure (a relationship likely to grow more consequential as climate change accelerates both coastal erosion and the intensity of the storms that help drive slope failure). As base-level lowering rates shift in response, terrain characterized by slow, comparatively manageable earthflow motion may face a growing susceptibility to the same transition toward rotational failure that has been documented in Big Sur. What our results ultimately suggest is not that earthflow terrain is secretly dangerous, but that hazard itself is a moving target whose trajectory depends on a hillslope's history as much as its geology.

REFERENCES

Alberti, S., Senogles, A., Kingen, K., et al. (2020). The Hooskanaden Landslide: Historic and recent surge behavior of an active earthflow on the Oregon Coast. *Landslides*, *17*, 2589–2602. https://doi.org/10.1007/s10346-020-01466-8

Balco, G., Finnegan, N. J., Gendaszek, A., Stone, J. O. H., & Thompson, N. (2013). Erosional response to northward-propagating crustal thickening in the coastal ranges of the U.S. Pacific Northwest. *American Journal of Science*. https://doi.org/10.2475/11.2013.01

Baum, R. L., Coe, J. A., Godt, J. W., et al. (2005). Regional landslide-hazard assessment for Seattle, Washington, USA. *Landslides*, *2*, 266–279. https://doi.org/10.1007/s10346-005-0023-y

Beacon Economics. (2025, September). *The economic impact of the 2023–2025 Highway 1 closures near Big Sur*. https://highway1roadtrip.com/wp-content/uploads/2025/10/HWY1ClosureEconomicImpactReport_2025.pdf

Bennett, G. L., Miller, S. R., Roering, J. J., & Schmidt, D. A. (2016). Landslides, threshold slopes, and the survival of relict terrain in the wake of the Mendocino Triple Junction. *Geology*, *44*(5), 363–366.

Berkland, J. O., Raymond, L. A., Kramer, J. C., Moores, E. M., & O'Day, M. (1972). What is Franciscan? *AAPG Bulletin*, *56*(12), 2295a–2302.

Bertolini, G., Guida, M., & Pizziolo, M. (2005). Landslides in Emilia-Romagna region (Italy): Strategies for hazard assessment and risk management. *Landslides*, *2*(4), 302–312.

Blake, M. C., Jr., & Jones, D. L. (1981). The Franciscan assemblage and related rocks in northern California: A reinterpretation. In W. G. Ernst (Ed.), *The geotectonic development of California* (pp. 306–329). Prentice-Hall.

Booth, A. M., & Roering, J. J. (2011). A 1-D mechanistic model for the evolution of earthflow-prone hillslopes. *Journal of Geophysical Research*, *116*(F4), Article F04021. https://doi.org/10.1029/2011JF002024

Brown, W. M., & Ritter, J. R. (1971). *Sediment transport and turbidity in the Eel River basin, California* (Water-Supply Paper 1986). U.S. Government Printing Office.

Burbank, D. W., Leland, J., Fielding, E., Anderson, R. S., Brozovic, N., Reid, M. R., & Duncan, C. (1996). Bedrock incision, rock uplift and threshold hillslopes in the northwestern Himalayas. *Nature*, *379*(6565), 505–510. https://doi.org/10.1038/379505a0

Burns, W. J., & Madin, I. P. (2009). *Protocol for inventory mapping of landslide deposits from light detection and ranging (LIDAR) imagery*. State Library of Oregon Digital Collections. https://digitalcollections.library.oregon.gov/nodes/view/184674

California Coastal Commission. (1987). *The California coastal resource guide*. University of California Press.

California Department of Transportation. (2018, Summer). Iconic Big Sur route reclaimed: Highway 1 crews have realigned, strengthened section after massive slide. *Mile Marker*, 30–31.

Clarke, S. H., Jr. (1992). Geology of the Eel River basin and adjacent region: Implications for late Cenozoic tectonics of the southern Cascadia subduction zone and Mendocino triple junction. *AAPG Bulletin*, *76*(2), 199–224.

Dawson, R. J., Dickson, M. E., Nicholls, R. J., Hall, J. W., Walkden, M. J., Stansby, P. K., Mokrech, M., Richards, J., Zhou, J., Milligan, J., Jordan, A., Pearson, S., Rees, J., Bates, P. D., Koukoulas, S., & Watkinson, A. R. (2009). Integrated analysis of risks of coastal flooding and cliff erosion under scenarios of long term change. *Climatic Change*, *95*(1–2), 249–288.

Desai, V. D., Handwerger, A. L., & Daniels, K. E. (2025). Using network science to evaluate landslide hazards on Big Sur Coast, California, USA. *Natural Hazards and Earth System Sciences*, *25*(12), 4755–4766.

Dickson, M. E., Walkden, M. J., & Hall, J. W. (2007). Systemic impacts of climate change on an eroding coastal region over the twenty-first century. *Climatic Change*, *84*(2), 141–166.

Dow, H. W., Warrick, J. A., & Ritchie, A. C. (2026). Patterns and drivers of cliff erosion in Big Sur, California, USA using repeat photogrammetry, 2017–2023. *Earth and Space Science*, *13*(5), Article e2025EA004595.

Ducea, M., House, M. A., & Kidder, S. (2003). Late Cenozoic denudation and uplift rates in the Santa Lucia Mountains, California. *Geology*, *31*(2), 139–142.

Fakrai, N. S., & Perkins, J. P. (2026). *Lidar-mapped landslides along the southern Big Sur Coast, CA* [Data set]. U.S. Geological Survey. https://doi.org/10.5066/P14TPSZL

Ferrier, K. L., Kirchner, J. W., & Finkel, R. C. (2005). Erosion rates over millennial and decadal timescales at Caspar Creek and Redwood Creek, northern California Coast Ranges. *Earth Surface Processes and Landforms*, *30*, 1025–1038.

Finnegan, N. J., Perkins, J. P., Nereson, A. L., & Handwerger, A. L. (2021). Unsaturated flow processes and the onset of seasonal deformation in slow-moving landslides. *Journal of Geophysical Research: Earth Surface*, *126*(5), Article e2020JF005758.

Finnegan, N. J., & Saffer, D. M. (2024). Seasonal slow slip in landslides as a window into the frictional rheology of creeping shear zones. *Science Advances*, *10*(42), Article eadq9399. https://doi.org/10.1126/sciadv.adq9399

Foster, M. A., & Kelsey, H. M. (2012). Knickpoint and knickzone formation and propagation, South Fork Eel River, northern California. *Geosphere*, *8*(2), 403–416.

Fuller, T. K., Perg, L. A., Willenbring, J. K., & Lepper, K. (2009). Field evidence for climate-driven changes in sediment supply leading to strath terrace formation. *Geology*, *37*(5), 467–470.

Gariano, S. L., & Guzzetti, F. (2016). Landslides in a changing climate. *Earth-Science Reviews*, *162*, 227–252.

Graymer, R. W., Langenheim, V. E., Roberts, M. A., & McDougall, K. (2014). *Geologic and geophysical maps of the eastern three-fourths of the Cambria 30′ × 60′ quadrangle, central California Coast Ranges* (Scientific Investigations Map 3287). U.S. Geological Survey. https://doi.org/10.3133/sim3287

Hahm, W. J., Rempe, D. M., Dralle, D. N., Dawson, T. E., Lovill, S. M., Bryk, A. B., ... Dietrich, W. E. (2019). Lithologically controlled subsurface critical zone thickness and water storage capacity determine regional plant community composition. *Water Resources Research*, *55*(4), 3028–3055.

Handwerger, A. L., Fielding, E. J., Sangha, S. S., & Bekaert, D. P. (2022). Landslide sensitivity and response to precipitation changes in wet and dry climates. *Geophysical Research Letters*, *49*(13), Article e2022GL099499.

Handwerger, A. L., Huang, M.-H., Fielding, E. J., Booth, A. M., & Bürgmann, R. (2019). A shift from drought to extreme rainfall drives a stable landslide to catastrophic failure. *Scientific Reports*, *9*(1), Article 1569. https://doi.org/10.1038/s41598-018-38300-0

Handwerger, A. L., Rempel, A. W., Skarbek, R. M., Roering, J. J., & Hilley, G. E. (2016). Rate-weakening friction characterizes both slow sliding and catastrophic failure of landslides. *Proceedings of the National Academy of Sciences*, *113*(37), 10281–10286. https://doi.org/10.1073/pnas.1607009113

Handwerger, A. L., Roering, J. J., & Schmidt, D. A. (2013). Controls on the seasonal deformation of slow-moving landslides. *Earth and Planetary Science Letters*, *377*, 239–247.

Handwerger, A. L., Roering, J. J., Schmidt, D. A., & Rempel, A. W. (2015). Kinematics of earthflows in the Northern California Coast Ranges using satellite interferometry. *Geomorphology*, *246*, 321–333.

Hapke, C., Green, K., & Dallas, K. (2004). *Maps showing estimated sediment yield from coastal landslides and active slope distribution along the Big Sur coast, Monterey and San Luis Obispo Counties, California* (Scientific Investigations Map 2852). U.S. Geological Survey. https://doi.org/10.3133/sim2852

Hapke, C. J., & Green, K. R. (2005). *Rates of landsliding and cliff retreat along the Big Sur coast, California—Measuring a crucial baseline* (Fact Sheet 2004-3099). U.S. Geological Survey. https://pubs.usgs.gov/fs/2004/3099/

Hapke, C. J., & Green, K. R. (2006). Coastal landslide material loss rates associated with severe climatic events. *Geology*, *34*(12), 1077.

Henson, P., & Usner, D. (2023a). Big Sur geology. In *The natural history of Big Sur* (pp. 7–31). University of California Press. https://doi.org/10.1525/9780520917798-006

Henson, P., & Usner, D. (2023b). Weather and climate. In *The natural history of Big Sur* (pp. 32–48). University of California Press. https://doi.org/10.1525/9780520917798-007

Huang, M.-H., Hudson-Rasmussen, B., Burdick, S., Lekic, V., Nelson, M. D., Fauria, K. E., & Schmerr, N. (2021). Bayesian seismic refraction inversion for critical zone science and near-surface applications. *Geochemistry, Geophysics, Geosystems*, *22*(5), Article e2020GC009172. https://doi.org/10.1029/2020GC009172

Hungr, O., Leroueil, S., & Picarelli, L. (2014). The Varnes classification of landslide types, an update. *Landslides*, *11*(2), 167–194.

Iverson, R. M. (2000). Landslide triggering by rain infiltration. *Water Resources Research*, *36*(7), 1897–1910. https://doi.org/10.1029/2000WR900090

Iverson, R. M., & Major, J. J. (1986). Groundwater seepage vectors and the potential for hillslope failure and debris flow mobilization. *Water Resources Research*, *22*(11), 1543–1548. https://doi.org/10.1029/WR022i011p01543

Jacquemart, M., & Tiampo, K. (2021). Leveraging time series analysis of radar coherence and normalized difference vegetation index ratios to characterize pre-failure activity of the Mud Creek landslide, California. *Natural Hazards and Earth System Sciences*, *21*(2), 629–642.

Johnson, S. Y., Watt, J. T., Hartwell, S. R., & Kluesner, J. W. (2018). Neotectonics of the Big Sur Bend, San Gregorio-Hosgri fault system, central California. *Tectonics*, *37*(6), 1930–1954. https://doi.org/10.1029/2017TC004724

Johnston, S. M., Singleton, J. S., Chapman, A. D., & Murray, G. (2019). Geologic map and structural development of the northernmost Sur-Nacimiento fault zone, central California coast. *Geosphere*, *15*(1), 171–187. https://doi.org/10.1130/GES02015.1

JPR Historical Consulting Services. (2001). *A history of road closures along Highway 1, Big Sur, Monterey and San Luis Obispo Counties, California*. California Department of Transportation. http://www.dot.ca.gov/dist05/projects/bigsur/inventory_reports/history_road_closures.pdf

Keefer, D. K., & Johnson, A. M. (1983). *Earth flows: Morphology, mobilization, and movement* (Professional Paper 1264). U.S. Geological Survey.

Kelsey, H. M. (1978). Earthflows in Franciscan melange, Van Duzen River basin, California. *Geology*, *6*(6), 361–364. https://doi.org/10.1130/0091-7613(1978)6<361:EIFMVD>2.0.CO;2

Kelsey, H. M. (1980). A sediment budget and an analysis of geomorphic process in the Van Duzen River basin, north coastal California, 1941–1975. *GSA Bulletin*, *91*, 1119–1216.

Kelsey, H. M., & Carver, G. A. (1988). Late Neogene and Quaternary tectonics associated with northward growth of the San Andreas transform fault, northern California. *Journal of Geophysical Research: Solid Earth*, *93*(B5), 4797–4819.

Kim, C. C., Snell, C., & Medley, E. (2004). Shear strength of Franciscan Complex melange as calculated from back-analysis of a landslide.

Komar, P. D. (1998). *Beach processes and sedimentation* (2nd ed.). Prentice Hall.

Lacroix, P., Handwerger, A. L., & Bièvre, G. (2020). Life and death of slow-moving landslides. *Nature Reviews Earth & Environment*, *1*(8), 404–419. https://doi.org/10.1038/s43017-020-0072-8

Leshchinsky, B., Olsen, M. J., Mohney, C., O'Banion, M., Bunn, M., Allan, J., & McClung, R. (2019). Quantifying the sensitivity of progressive landslide movements to failure geometry, undercutting processes and hydrological changes. *Journal of Geophysical Research: Earth Surface*, *124*(2), 616–638. https://doi.org/10.1029/2018JF004833

Limber, P. W., Barnard, P. L., Vitousek, S., & Erikson, L. H. (2018). A model ensemble for projecting multidecadal coastal cliff retreat during the 21st century. *Journal of Geophysical Research: Earth Surface*, *123*(7), 1566–1589.

Lindquist, E. S., & Goodman, R. E. (1994). Strength and deformation properties of a physical model melange.

Lock, J., Kelsey, H., Furlong, K., & Woolace, A. (2006). Late Neogene and Quaternary landscape evolution of the northern California Coast Ranges: Evidence for Mendocino triple junction tectonics. *Geological Society of America Bulletin*, *118*(9–10), 1232–1246.

Mackey, B. H., & Roering, J. J. (2011). Sediment yield, spatial characteristics, and the long-term evolution of active earthflows determined from airborne LiDAR and historical aerial photographs, Eel River, California. *GSA Bulletin*, *123*(7–8), 1560–1576.

Mansour, M. F., Morgenstern, N. R., & Martin, C. D. (2011). Expected damage from displacement of slow-moving slides. *Landslides*, *8*(1), 117–131.

Martel, S. J. (2004). Mechanics of landslide initiation as a shear fracture phenomenon. *Marine Geology*, *203*(3–4), 319–339.

McLaughlin, R. J., Ellen, S. D., Blake, M. C., Jr., Jayko, A. S., Irwin, W. P., Aalto, K. R., ... Cyr, K. A. (2000). *Geology of the Cape Mendocino, Eureka, Garberville, and southwestern part of the Hayfork 30' × 60' quadrangles and adjacent offshore area, northern California* (Miscellaneous Field Studies Map MF-2336, scale 1:100,000). U.S. Geological Survey.

Medley, E. W. (2001). Orderly characterization of chaotic Franciscan melanges. *Felsbau*, *19*(4), 20–33.

Merritts, D. J. (1996). The Mendocino triple junction: Active faults, episodic coastal emergence, and rapid uplift. *Journal of Geophysical Research*, *101*(B3), 6051–6070.

Merritts, D. J., & Bull, W. B. (1989). Interpreting Quaternary uplift rates at the Mendocino triple junction, northern California, from uplifted marine terraces. *Geology*, *17*, 1020–1024.

Murphy, C. R., Finnegan, N. J., & Oberle, F. K. J. (2022). Vadose zone thickness limits pore-fluid pressure rise in a large, slow-moving earthflow. *Journal of Geophysical Research: Earth Surface*, *127*, Article e2021JF006415.

Ohlmacher, G. C. (2007). Plan curvature and landslide probability in regions dominated by earth flows and earth slides. *Engineering Geology*, *91*(2–4), 117–134.

OpenTopography. (n.d.). *Eel River, CA: Landsliding and the evolution of mountainous landscapes* [Data set]. https://doi.org/10.5069/G9XS5S9P

Raymond, L. A. (2018). What is Franciscan?: Revisited. *International Geology Review*, *60*(16), 1968–2030. https://doi.org/10.1080/00206814.2017.1396933

Roering, J. J., Mackey, B. H., Handwerger, A. L., Booth, A. M., Schmidt, D. A., Bennett, G. L., & Cerovski-Darriau, C. (2015). Beyond the angle of repose: A review and synthesis of landslide processes in response to rapid uplift, Eel River, Northern California. *Geomorphology*, *236*, 109–131.

Roering, J. J., Stimely, L. L., Mackey, B. H., & Schmidt, D. A. (2009). Using DInSAR, airborne LiDAR, and archival air photos to quantify landsliding and sediment transport. *Geophysical Research Letters*, *36*(19), Article L19402. https://doi.org/10.1029/2009GL040374

Rocscience Inc. (2024). *RS2* (Version 12.0) [Computer software]. Rocscience.

Schmidt, K. M., & Montgomery, D. R. (1995). Limits to relief. *Science*, *270*(5236), 617–620.

Schulz, W. H. (2004). *Landslides mapped using LIDAR imagery, Seattle, Washington* (Open-File Report 2004-1396). U.S. Geological Survey.

Snyder, N. P., Whipple, K. X., Tucker, G. E., & Merritts, D. J. (2000). Landscape response to tectonic forcing: Digital elevation model analysis of stream profiles in the Mendocino triple junction region, northern California. *GSA Bulletin*, *112*, 1250–1263.

Steely, A. N. (2016). *Fault-controlled patterns of uplift in the central California Coast Range and laser-ablation depth-profile analysis of zircon* [Doctoral dissertation, University of California, Santa Cruz]. eScholarship.

U.S. Geological Survey. (2024). *1 meter Digital Elevation Models (DEMs)—USGS National Map 3D Elevation Program (3DEP) downloadable data collection* [Data set]. https://www.sciencebase.gov/catalog/item/543e6b86e4b0fd76af69cf4c

Varnes, D. J. (1978). Slope movement types and processes. In R. L. Schuster & R. J. Krizek (Eds.), *Landslides: Analysis and control* (Special Report 176, pp. 11–33). Transportation Research Board, National Academy of Sciences.

Walkinshaw, J. (1992). Landslide correction costs on US state highway systems. *Transportation Research Record*, 36.

Warrick, J. A., Ritchie, A. C., Schmidt, K. M., et al. (2019). Characterizing the catastrophic 2017 Mud Creek landslide, California, using repeat structure-from-motion (SfM) photogrammetry. *Landslides*, *16*, 1201–1219. https://doi.org/10.1007/s10346-019-01160-4

Willenbring, J. K., Gasparini, N. M., Crosby, B. T., & Brocard, G. (2013). What does a mean mean? The temporal evolution of detrital cosmogenic denudation rates in a transient landscape. *Geology*, *41*(12), 1215–1218. https://doi.org/10.1130/G34746.1

Wills, C. J., Manson, M. W., Brown, K. D., Davenport, C. W., & Domrose, C. J. (2001). *Special Report 185—Landslides in the Highway 1 corridor: Geology and slope stability along the Big Sur coast between Point Lobos and San Carpoforo Creek, Monterey and San Luis Obispo Counties, California*. California Department of Conservation, California Geological Survey.

Winter, S., Handwerger, A. L., & Fielding, E. J. (2024). *Defining precursors of ground failure: A weather-dependent multiscale framework for early landslide prediction through geomechanics and remote sensing* [Internal report]. NASA Jet Propulsion Laboratory.

Xu, Y., Schulz, W. H., Lu, Z., Kim, J., & Baxstrom, K. (2021). Geologic controls of slow-moving landslides near the US West Coast. *Landslides*, *18*(10), 3353–3365.

Young, H. H., & Hilley, G. E. (2018). Millennial-scale denudation rates of the Santa Lucia Mountains, California: Implications for landscape evolution in steep, high-relief, coastal mountain ranges. *GSA Bulletin*, *130*(11–12), 1809–1824. https://doi.org/10.1130/B31907.1